J. Mech. Phys. Solids Vol. 40, No. 3, pp. 485–509, 1992.
Printed in Great Britain.

0022–5096/92 $5.00+0.00

MODE MIXITY EFFECT ON THE DAMAGE OF A CONSTRAINED DUCTILE LAYER

A. G. VARIAS,† Z. SUO‡ and C. F. SHIH†§

† Division of Engineering, Brown University, Providence, RI 02912, U.S.A., and ‡ Department of Mechanical Engineering, University of California, Santa Barbara, CA 93106, U.S.A.

(*Received* 18 *December* 1990; *in revised form* 21 *June* 1991)

ABSTRACT

A PARTIALLY fractured thin metal foil bonded between ceramic blocks subject to mode I loading was studied in a previous paper. The constrained plastic flow easily elevates the hydrostatic stress in the metal to more than 5 times the yield stress. The maximum stress occurs at a distance of several foil thicknesses ahead of the crack tip, and can trigger cavitation or debonding. The large spacing between the cavities and the crack tip allows the intact metal patches to bridge the crack, leading to rising crack growth resistance curves. The maximum foil thickness which would allow the above bridging mechanism to develop has been identified. In this paper mode mixity effects are investigated. As the mode II component increases, the plastic zone becomes longer while the stress triaxiality becomes smaller. The loss of constraint is detailed in this paper. Under mixed-mode loading, high tensile stresses also occur in the ceramics. These stresses are large enough to cause ceramic cleavage. Using a full-field large-deformation elastic–plastic analysis, the multi-mechanism competition is assessed. The dependence of nominal fracture toughness on failure mechanisms and on geometric and material parameters is also discussed.

1. INTRODUCTION

VARIOUS advanced composites have been explored in recent years. Composites are fabricated using ceramics, intermetallics, metals and polymers, with a variety of architectures: fiber, whisker, particle, platelet, network and sheet. One category consists of laminates with alternate metal and ceramic layers. When these composites are loaded, the plastic deformation in the metal is constrained by the surrounding ceramics, which in turn elevates the hydrostatic stress. The high stresses can trigger several failure mechanisms that would not operate under unconstrained plastic flow. One mechanism of particular interest is high triaxiality induced cavitation (ASHBY *et al.*, 1989).

REIMANIS *et al.* (1991) have carried out fracture experiments with gold foils diffusion bonded between sapphire plates. The crack geometry is shown in Fig. 1(a). The foil thickness, h, is much smaller than the overall dimension of the specimen. During loading, interfacial cavities develop at a distance several times the foil thickness

§ Author to whom correspondence should be addressed.

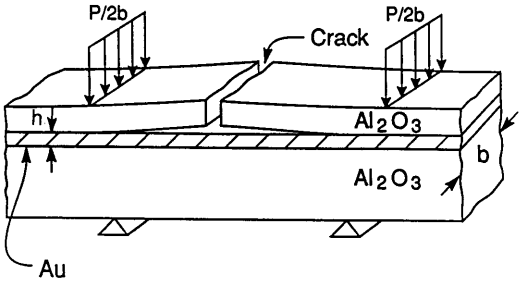

FIG. 1(a). Four-point bend specimen made of gold foil bonded between sapphire plates used in the experiments of REIMANIS *et al.* (1991). The foil thickness is much smaller than that of the plates.

ahead of the crack tip; these cavities do not connect with the crack tip [Fig. 1(b)]. With further loading, new cavities nucleate at an even larger distance ahead of the crack tip [Fig. 1(c)]. Cavities also appear at the other interface (not shown in Fig. 1). The intact metal ligaments bridge the crack. The growth of the bridging zone results in rapidly rising crack growth resistance curves (*R*-curves). Further modeling along this line is given in SUO *et al.* (1992). In this paper we focus on the mechanism of cavitation that is the precursor to the bridging.

A finite element analysis of VARIAS *et al.* (1991) reveals that the hydrostatic stress in the metal foil can easily exceed 5 times its yield stress. Such high stresses at a distance of several foil thickness ahead of the crack tip can cause cavitation at those locations. An event that may intervene is ductile crack growth. As an example, consider the gold–sapphire system mentioned above. The energy release rate, corresponding to a mean stress of 5.5 times the yield stress of the metal σ_0, is given by

$$\mathcal{G}_{\text{cavity}} = 0.2\sigma_0 h,$$

where h is the foil thickness. This high mean stress level is assumed to be sufficient to cause cavitation. On the other hand, $\mathcal{G}$ is also related to the crack opening displacement δ_t:

$$\mathcal{G} = 1.8\sigma_0\delta_t.$$

We assume that the blunted crack will grow when the pores or other processing flaws are subject to intensive straining. Let X_0 be the mean flaw spacing. Since the intensive strain occurs within a distance δ_t ahead of the crack tip, the condition for near-tip cavity growth and coalescence with the tip can be stated as $\delta_t \approx X_0$. Thus the energy release rate needed for the crack to grow is

$$\mathcal{G}_{\text{growth}} = 1.8\sigma_0 X_0.$$

If $\mathcal{G}_{\text{cavity}} < \mathcal{G}_{\text{growth}}$ cavitation is the operative mechanism. Based on the two estimates given above, we conclude that the cavity formation is favored if

$$h < 9X_0.$$

In other words, the formation of a cavitation bridging zone is ensured by a foil which is thin relative to the mean flaw spacing. However, a very thin foil does not

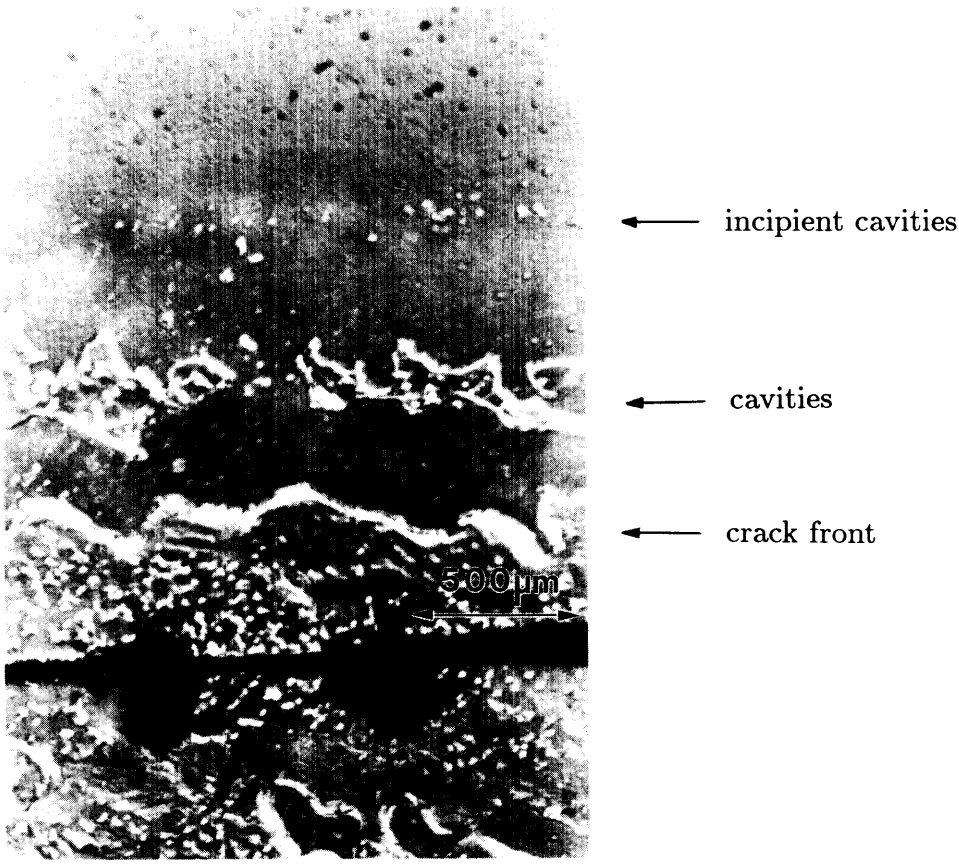

FIG. 1(b). An array of interfacial cavities has developed ahead of the crack front. An array of incipient cavities lies further ahead. The gold layer thickness is 25 μm. The photograph is taken from the top side of the specimen through the transparent sapphire.

FIG. 1(c). The second array of interfacial cavities has grown with the increase in the applied loading.

contribute much ductility to the bridging mechanism so that the increase in fracture resistance is limited. A foil thickness close to the critical thickness given above is optimum for improving the fracture resistance of the layered material. The above results were obtained for mode I loading, where the metal foil is most severely constrained.

In this paper, we study the loss of constraint due to the mode II load component. As in the previous study, the fields which bear on the competition are obtained with large-deformation elastic–plastic analysis. We found that the mixed-mode loading significantly alters the near-tip field. The implications on the nominal fracture toughness is discussed. The effect of the crack position on the stress field is considered in the Appendix, where an interface crack is analyzed. Appropriately interpreted, the results for an interface crack are similar to those for the crack lying in the mid-plane of the foil, thus reinforcing the findings in the main section.

2. Boundary Value Problem

The boundary value problem to be analyzed is shown in Fig. 2. A metal foil of thickness h is bonded between two identical ceramic substrates. Young's moduli and Poisson's ratios are E and ν for the foil, and E_s and ν_s for the substrates. The metal deforms according to the finite-strain J_2 flow theory:

$$\dot{\bar{\varepsilon}}^p = \dot{\varepsilon}_0 \left[\frac{\bar{\sigma}}{H(\bar{\varepsilon}^p)}\right]^{1/m}, \quad H(\bar{\varepsilon}^p) = \sigma_0 \left(1 + \frac{\bar{\varepsilon}^p}{\varepsilon_0}\right)^{1/n}, \tag{1}$$

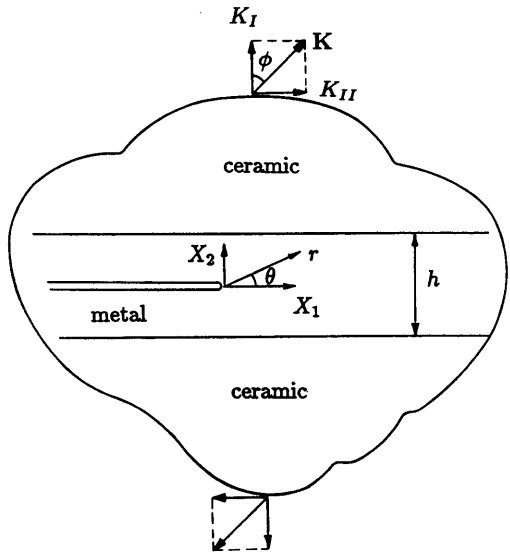

FIG. 2. Metal foil bonded between two ceramic substrates, with a centerline crack. The elastic K-field is applied at distance $r \gg h$.

where n is the strain hardening exponent, σ_0 the initial yield stress, $\bar{\sigma}$ the effective stress, $\bar{\varepsilon}^p$ and $\dot{\bar{\varepsilon}}^p$ the equivalent plastic strain and strain rate, and ε_0 $(= \sigma_0/E)$ and $\dot{\varepsilon}_0$ the reference strain and strain rate. The strain rate sensitivity m is assigned a value of 0.005 and the loading rate is sufficiently smooth so that the constitutive response pertains to a rate-independent material. A detailed constitutive description was given in VARIAS *et al.* (1991). The results presented in the following are for a ceramic–metal with properties

$$E/\sigma_0 = 300, \quad n = 10, \quad \nu = 0.33, \quad \nu_s = 0.2, \quad E_s/E = 5. \tag{2}$$

However, the overall features should be considered generic.

A crack lies along the centerline of the foil. The foil is thin compared to the overall specimen dimension, so that the plane strain deformation prevails. In the substrates far from the metal foil, the stress field conforms to the homogeneous mixed-mode elastic crack-tip field

$$\sigma_{ij}(r,\theta) \sim \frac{K_I}{\sqrt{2\pi r}} f_{ij}^I(\theta) + \frac{K_{II}}{\sqrt{2\pi r}} f_{ij}^{II}(\theta), \quad r \gg h, \tag{3}$$

where the angular functions f_{ij} can be found in fracture mechanics textbooks. As a convention we write

$$\mathbf{K} = K_I + iK_{II} = |\mathbf{K}|\, e^{i\phi}. \tag{4}$$

The loading phase ϕ varies from 0 to $\pi/2$, corresponding to a change from mode I to mode II. For the four-point flexural specimen in Fig. 1(a), the loading phase is $\phi \simeq \pi/4$. Figure 3 shows the mesh in our calculations. The layer thickness was taken to be $40b_0$, where b_0 is the initial distance between points A and B, as shown in Fig. 3(a). Calculations were performed for $R/h = 500$, 1000 and 5000, where R is the radius to the boundary where the elastic K-field (3) is applied.

3. STRUCTURE OF FIELDS

3.1. *Form of stress distribution*

Consider a semi-infinite crack in a *homogeneous* material subject to remote tractions (3). The fields depend on distance only through $r/(|\mathbf{K}|/\sigma_0)^2$. The self-similar fields are members of a family parameterized by the mode mixity ϕ, i.e.

$$\sigma_{ij} = \sigma_0 h_{ij}\left(\frac{r}{(|\mathbf{K}|/\sigma_0)^2}, \theta; \phi\right). \tag{5}$$

The above form is valid everywhere including the zone of finite strains. Mode I near-tip fields under finite strain have been discussed by RICE and JOHNSON (1970) and MCMEEKING (1977), mixed-mode fields by AOKI *et al.* (1987) and BUDDEN (1987, 1988), and small-strain mixed-mode fields by SHIH (1974).

In our study the plastic zone size, r_p, is defined as the maximum distance of the effective plastic strain contour $\bar{\varepsilon}^p = 0.001$ from the crack tip. The crack-tip displace-

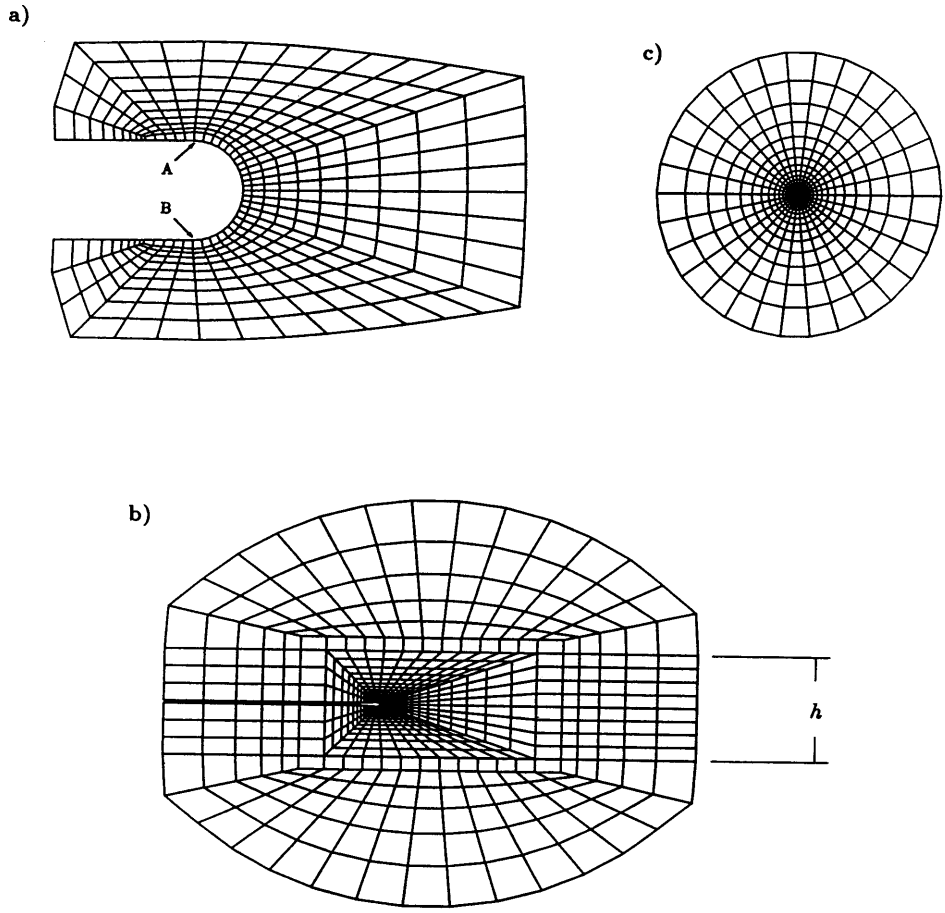

FIG. 3. Finite element meshes. (a) Near-tip mesh. (b) The strip represents the metal foil. (c) Far-field mesh. The elastic K-field is applied along the outer circular boundary.

ment, δ_t, is defined as the relative displacement of points A and B shown in Fig. 3(a). Note that $\delta_t \approx \varepsilon_0 r_p$.

Now consider the problem in Fig. 2. The problem has one geometric length, h, which is fixed. By dimensionality, $|\mathbf{K}|/(\sigma_0\sqrt{h})$ measures the applied load. This proves to be a convenient load parameter for this study. We direct attention to the ductile layer and vicinity.

Consider the stress profile along the center line. The field is of the form

$$\sigma_{ij} = \sigma_0 q_{ij}\left(\frac{X_1}{(|\mathbf{K}|/\sigma_0)^2}; \frac{|\mathbf{K}|}{\sigma_0\sqrt{h}}, \phi\right), \tag{6}$$

where q_{ij} depends additionally on material properties. The details of this field for $\phi = 0$ are given in VARIAS *et al.* (1991). Three cases are distinguished:

Case i: $r_p \ll h$

For a small plastic zone, $r_p \ll h$, an inner K-field surrounds the tip. By an application of the J-integral (RICE, 1968) the magnitude of $|\mathbf{K}|^{\text{tip}}$ is related to $|\mathbf{K}|$ by

$$|\mathbf{K}|^{\text{tip}} = \left[\frac{E}{E_s}\left(\frac{1-\nu_s^2}{1-\nu^2}\right)\right]^{1/2}|\mathbf{K}|. \tag{7}$$

Field (5) holds everywhere within the plastic zone.

Case ii: $\delta_t \ll h$, **and** $r_p \geqslant h$

Here an inner K-field does not exist. Nevertheless the form in (5) applies for distances $r < h$.

Case iii: $\delta_t < h$, **and** $r_p \gg h$

For this case the form in (5) does not apply anywhere in the constrained layer. We will focus our attention on the latter two cases.

3.2. *Evolution of high stresses at* $X_1 \geqslant h$

The evolution of the mean stress in the constrained layer, the maximum tensile stress in the ceramic and the normal interfacial traction are considered in this section. Since these stresss obey form (6), the subsequent discussion applies to all of them. For convenience the stress is denoted by σ and the identification with specific stress quantities can be made later.

We multiply both sides of (6) by the dimensionless load $(\sigma_0\sqrt{h})/|\mathbf{K}|$ and rearrange to get

$$\frac{\sigma\sqrt{h}}{|\mathbf{K}|} = \frac{\sigma_0\sqrt{h}}{|\mathbf{K}|}\cdot f\left(\frac{\sigma_0\sqrt{X_1}}{|\mathbf{K}|}; \frac{|\mathbf{K}|}{\sigma_0\sqrt{h}}, \phi\right). \tag{8}$$

Suppose the maximum stress, σ^*, develops at a distance $X_1 \approx h$. Using this in (8), we obtain the form

$$\frac{|\mathbf{K}|}{\sigma^*\sqrt{h}} = F\left(\frac{|\mathbf{K}|}{\sigma_0\sqrt{h}}; \phi\right). \tag{9}$$

Expand the function in (9) about zero load with respect to the load parameter to get

$$\frac{|\mathbf{K}|}{\sigma^*\sqrt{h}} = F(0,\phi) + \frac{\partial F(0,\phi)}{\partial(|\mathbf{K}|/\sigma_0\sqrt{h})}\frac{|\mathbf{K}|}{\sigma_0\sqrt{h}} + \frac{\partial^2 F(0,\phi)}{\partial(|\mathbf{K}|/\sigma_0\sqrt{h})^2}\left(\frac{|\mathbf{K}|}{\sigma_0\sqrt{h}}\right)^2 + \cdots \tag{10}$$

When plastic strains are comparable to elastic strains in the neighborhood of the maximum stress, a one-term expansion adequately describes the behavior of σ^*. We write

$$\frac{|\mathbf{K}|}{\sigma^*\sqrt{h}} \sim B(\phi). \tag{11}$$

In this case σ^* increases linearly with $|\mathbf{K}|/(\sigma_0\sqrt{h})$. It can be shown that $\delta_t \ll h$ is in the "low load range" adequately represented by a one-term expansion.

In a less constrained deformation mode, e.g. $|\phi| > \pi/6$, the maximum stress develops in the region where plastic strains are significantly larger than elastic strains. The plastic deformation and the blunting of the tip, which is now a sizable fraction of h, reduce the rate of elevation of the stress. Such effects can be accounted for by the second term in (10). That is, the two-term expansion

$$\frac{|\mathbf{K}|}{\sigma^*\sqrt{h}} \sim B(\phi) + A(\phi)\frac{|\mathbf{K}|}{\sigma_0\sqrt{h}} \tag{12}$$

can account for the stress increase due to the elastic response to the applied load, and the stress relaxation caused by large-scale plasticity and crack-tip blunting.

The role of the second term can be appreciated by considering the near-tip fields in a homogeneous material. With h interpreted as the blunted opening of the tip, we get $\sigma^*/\sigma_0 \sim 1/A(\phi)$. That is, at large $|\mathbf{K}|/\sigma_0\sqrt{\delta_t}$ the stress approaches the asymptotic value $1/A(\phi)$ which depends on mode mixity. This behavior is consistent with a well-known result that the blunted tip limits the stress that can be achieved ahead of the crack to a finite value (RICE and JOHNSON, 1970; MCMEEKING, 1977; AOKI *et al.*, 1987; BUDDEN, 1987, 1988).

The validity of (12) has been confirmed by our numerical calculations. Over the full range of mode mixity and plastic zone sizes up to $400h$, relation (12) predicts the evolution of the maximum stresses to an accuracy better than 2%. At the very large plastic zones analyzed, the crack tip has opened to a width of nearly $h/2$.

A more convenient form of (12) for our purpose is

$$\frac{\sigma^*}{\sigma_0} = \frac{|\mathbf{K}|/(\sigma_0\sqrt{h})}{A|\mathbf{K}|/(\sigma_0\sqrt{h}) + B}. \tag{13}$$

It is easily seen that σ^*/σ_0 approaches the value $1/A$ at large $|\mathbf{K}|/(\sigma_0\sqrt{h})$, i.e.

$$\left(\frac{\sigma^*}{\sigma_0}\right) < \frac{1}{A(\phi)}. \tag{14}$$

The values of $A(\phi)$ and $B(\phi)$ are given in Table 1. In Table 1, the subscripts C, N and A denote values appropriate to the tensile stress $\sigma_\dagger^*$ in the elastic substrate, the mean stress σ_m^* in the ductile layer, and the normal interfacial traction σ_{22}^*, respectively. It is of interest that, for $\phi = 0$, the asymptotic value of σ^*/σ_0 is 40. For $\phi = \pi/4$, the asymptotic value of σ^*/σ_0 is 7.

3.3. *Plastic zone size and crack-tip displacement*

To complete this section, we provide relations for the plastic zone size and the crack-tip displacement. Under mixed-mode loading,

TABLE 1. *Parameters governing the elevation of stress maxima given by* (13): $\sigma_m^* =$ *maximum mean stress in the foil,* $\sigma_{22}^* =$ *maximum normal interfacial traction,* $\sigma_1^* =$ *maximum principal stress in the elastic substrate*

	σ_1^*		σ_m^*		σ_{22}^*	
ϕ	A_C	B_C	A_N	B_N	A_A	B_A
0	0.037	2.276	0.025	2.766	0.037	2.276
$\pi/6$	0.067	1.628	0.091	2.470	0.108	2.054
$\pi/4$	0.111	1.221	0.142	2.987	0.195	2.185
$\pi/3$	0.134	1.158	0.223	3.932	0.301	2.987
$\pi/2$	0.236	1.016	1.626	3.676	2.712	2.914

$$r_p = \Lambda |\mathbf{K}|^2/\sigma_0^2. \tag{15}$$

In general, the dimensionless number Λ depends on mode mixity ϕ and the dimensionless foil thickness, $h/(|\mathbf{K}|/\sigma_0)^2$. For $r_p \ll h$, Λ depends only on ϕ and is given by mixed-mode solutions to the homogeneous medium, after taking (7) into account, as in SHIH (1974). For $r_p \gg h$, Λ depends again only on ϕ, but the values are smaller than those for unconstrained plastic zone growth.

The crack-tip displacement has the form

$$\delta_t = d(J/\sigma_0) = (1-\nu_s^2)\varepsilon_0(dE/E_s)|\mathbf{K}|^2/\sigma_0^2, \tag{16}$$

where $J = (1-\nu_s^2)|\mathbf{K}|^2/E_s$ and d depends on ϕ and weakly on $|\mathbf{K}|/(\sigma_0\sqrt{h})$. This is a generalization of the result in SHIH (1981). The additional dependence of d on material properties is noted.

4. STRESS AND DEFORMATION FIELDS

4.1. *Pattern of fields*

At low loads producing plastic zones which are small compared to the layer thickness, the fields within the plastic zone are identical to those of a crack in a homogeneous ductile material. As the load is increased the plastic zone, growing at a rate given by (15), eventually reaches the interfaces. Upon reaching the boundaries at $X_2 = \pm h/2$, the plastic zone is constrained by the elastic substrates to extend only in the X_1-direction. At this stage and beyond, the plastic zone growth rate is reduced and the character of the stress field changes. The overall stress level gradually elevates and a second maximum stress develops at a distance of about h ahead of the tip. As the remote load increases further, the maximum stress builds up to very high levels as its location shifts to larger distances ahead of the crack tip.

We begin by examining the fields that develop under mode I loading, $\phi = 0$. Contour plots in Fig. 4 for $\bar{\varepsilon}^p$ and the mean stress, $\sigma_m = (\sigma_{11}+\sigma_{22}+\sigma_{33})/3$, are representative of the pattern of the fields that develop under constrained plastic flow for $r_p > h$. Note that the mean stress has reached $5\sigma_0$ at $X_1 = 2h$ ahead of the tip [see Fig. 4(b)]. Within the layer, the high stresses show little variation with X_2.

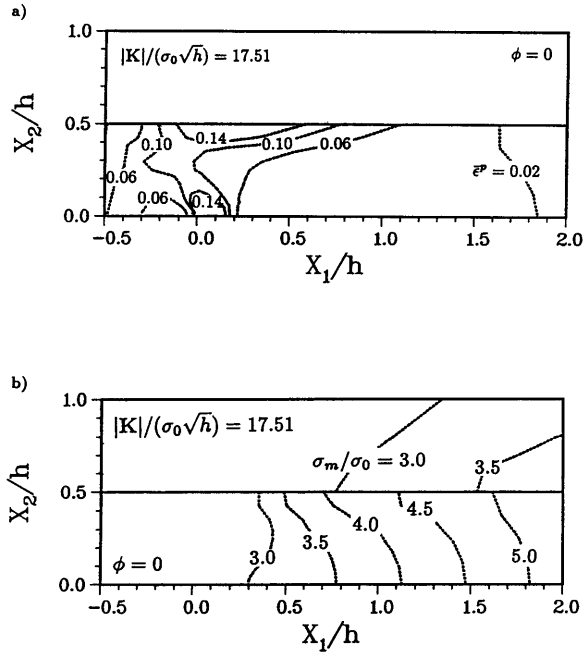

FIG. 4. Contours of: (a) effective plastic strain, and (b) stress triaxiality for $\phi = 0$. $K_I/(\sigma_0\sqrt{h}) = 17.51$.

Under mixed-mode loading, $\pi/6 \leqslant \phi \leqslant \pi/3$, the forward (and dominant) lobe of the plastic zone advances in a direction more closely aligned to the X_1-axis. The smaller lobe advances in the $-X_2$-direction. Upon impinging the elastic substrates the growth of the plastic zone is constrained, but to a lesser degree than that in mode I. The fields corresponding to mode mixity $\phi = \pi/4$ are shown in Fig. 5. The contours of $\bar{\varepsilon}^p$ and σ_m are representative of fields that develop for $r_p \gg h$. The hydrostatic stress reaches nearly $3\sigma_0$ at $X_1 \approx h$ at the lower boundary $X_2 = -h/2$ [see Fig. 5(b)]. The stress magnitudes decrease moderately with distance away from the lower boundary.

The spatial distribution of $\bar{\varepsilon}^p$ and σ_m under mode II loading for $r_p \gg h$ is shown in Fig. 6. In this case it is clear that the plastic zone growth is unconstrained. With the exception of the crack-tip region, σ_m does not exceed the yield stress anywhere in the layer.

4.2. *Stress distribution*

The mean stress in the ductile layer for different mode mixities, $\phi = 0$, $\pi/6$, $\pi/4$ and $\pi/3$, are compared in Fig. 7 at the same level of applied load. It can be seen that as mode mixity shifts away from mode I the high stress elevation is significantly reduced and its location is closer to the tip.

To understand the behavior of the field under mixed-mode conditions, the mean stress distribution for $\phi = \pi/4$ is shown in Fig. 8(a) for four different levels of the

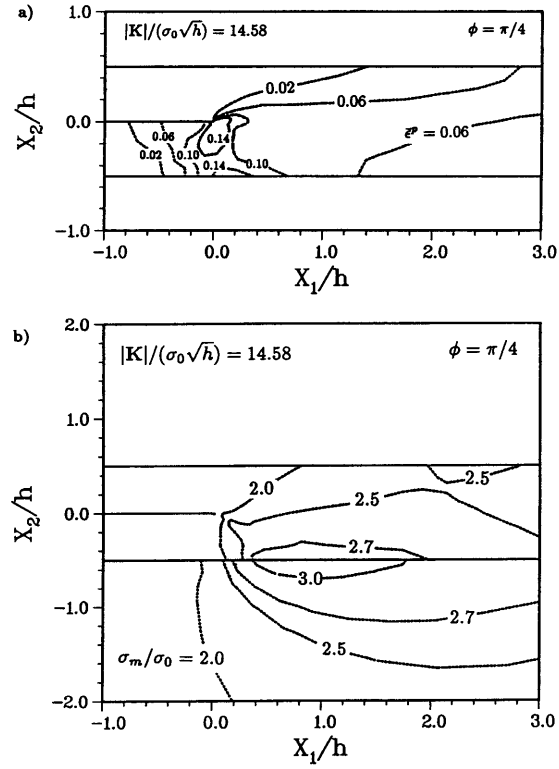

FIG. 5. Contours of: (a) effective plastic strain, and (b) stress triaxiality for $\phi = \pi/4$. $|\mathbf{K}|/(\sigma_0\sqrt{h}) = 14.58$.

applied load. The distribution vs the similarity coordinate $X_1/(|\mathbf{K}|/\sigma_0)^2$ is shown in Fig. 8(b). The latter scaling compresses the spatial distance as the load increases. Beyond the region of peak stresses, the stress distributions merge into a single distribution. Though not shown, similar distributions are observed for the other mode mixities. The distribution for $\phi = 0$ is shown in an earlier paper (VARIAS *et al.*, 1991). The other stress quantities also follow these trends. These field distributions support our observation that the fields for $X_1 > h$ are given by the form in (6).

Under mixed-mode loading, $\phi > 0$, high stresses develop along the boundary $X_2 = -h/2$. (For $\phi < 0$, high stresses develop at the other boundary $X_2 = h/2$.) Figure 9(a) shows the X_1-distribution of the mean stress in the ductile layer, the maximum (tensile) principal stress σ_1 in the ceramic and the normal and shear interfacial tractions, σ_{22} and σ_{12}. The mean stress and the normal interface traction are equal in magnitude but the tensile stress in the ceramic is about twice as large. For comparison purposes the stresses for mode I loading are shown in Fig. 9(b). Here σ_m^*, σ_1^* and σ_{22}^* are comparable in magnitude. These distributions suggest that, as the relative proportion of mode II loading increases, the likelihood of ceramic fracture also increases. Values of σ_m^*, σ_{22}^* and σ_1^* for several values of $|\mathbf{K}|/(\sigma_0\sqrt{h})$ are tabulated in Table 2 for four mode mixities.

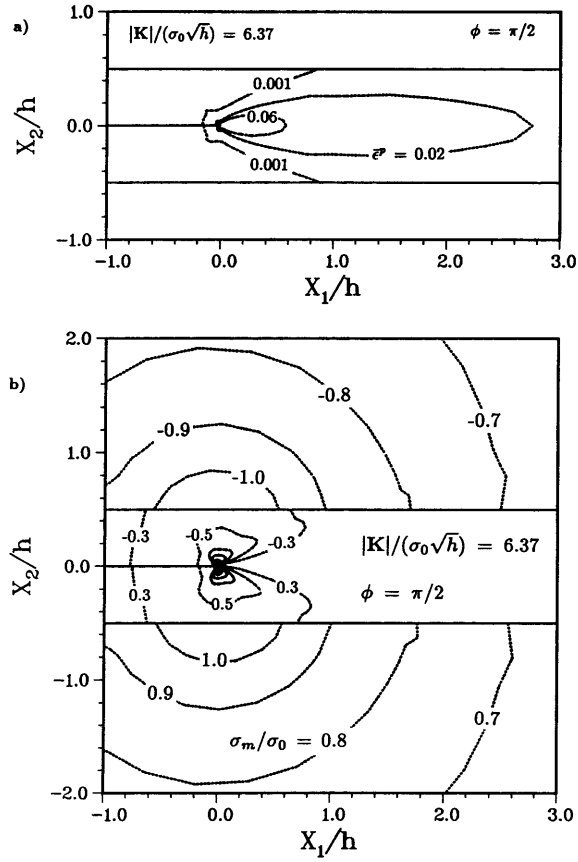

FIG. 6. Contours of: (a) effective plastic strain, and (b) stress triaxiality for $\phi = \pi/2$. $|\mathbf{K}|/(\sigma_0\sqrt{h}) = 6.37$.

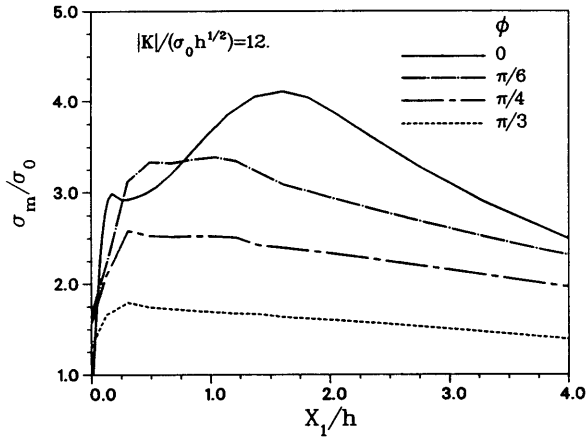

FIG. 7. Comparison of mean stress distributions in the metal foil for four mode mixities. For mode I the distribution is along the centerline and for mixed modes along the lower interface.

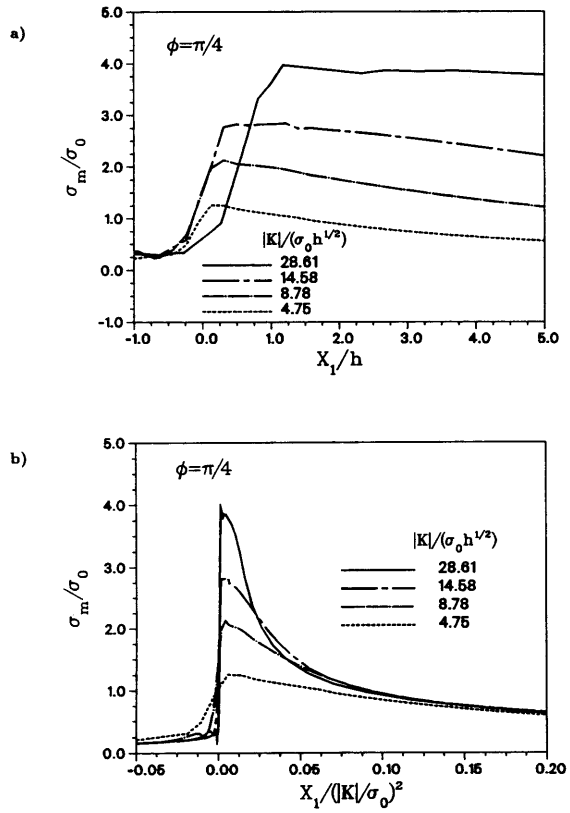

FIG. 8. Comparison of mean stress distributions along the lower interface for four applied loads. $\phi = \pi/4$. (a) Distance normalized by layer thickness. (b) Distance normalized by $(|\mathbf{K}|/\sigma_0)^2$.

4.3. *Growth of plastic zone*

The growth of the plastic zone r_p with applied load $|\mathbf{K}|/(\sigma_0\sqrt{h})$ is shown in Fig. 10(a) for five mode mixities. It can be seen that the rate of growth is much larger for mixed-mode loading. The ratio $r_p/(|\mathbf{K}|/\sigma_0)^2$ ($\equiv \Lambda$) vs r_p/h is shown in Fig. 10(b). At large r_p/h these ratios approach limiting values which depend on the mode mixity ϕ. For $\phi = 0$, $\pi/3$, $\pi/4$, $\pi/3$ and $\pi/2$, the limiting values of Λ are 0.025, 0.26, 0.49, 0.74 and 0.88 (estimated), respectively. The corresponding values of Λ for a homogeneous material, estimated from SHIH (1974), are 0.15, 0.32, 0.52, 0.75 and 0.88. Under mode I conditions, the effect of elastic substrates is to reduce the plastic zone size by a factor of 6.

4.4. *Near-tip plastic deformation*

The deformed shape of the crack tip is shown in Fig. 11. As the relative proportion of mode II increases, blunting develops at the lower crack zone. In contrast, the upper crack-tip zone becomes sharper and sharper. (The deformation pattern is reversed for

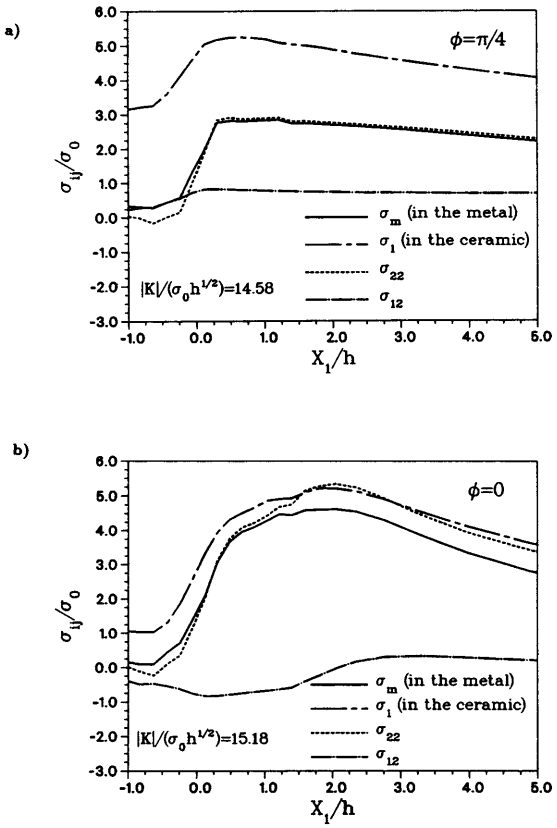

FIG. 9. Stress distributions along the interface. (a) $\phi = \pi/4$, $X_2 = -h/2$; (b) $\phi = 0$, $X_2 = h/2$.

$\phi < 0$.) Similar features were observed in bulk homogeneous ductile material (AOKI *et al.*, 1987).

In Section 3.3 we argued that δ_t, defined as the relative displacement of points A and B shown in Fig. 3(a), is scaled by $(|\mathbf{K}|/\sigma_0)^2$. The ratio $\delta_t/(|\mathbf{K}|/\sigma_0)^2$ is tabulated in Tables 2a–d for a range of $|\mathbf{K}|$s. The calculated ratios demonstrate the weak dependence of d on $|\mathbf{K}|/(\sigma_0\sqrt{h})$. The displacement δ_t sets the spatial extent over which large strain develops and this has implications on near-tip failure mechanisms.

5. DAMAGE NUCLEATION AND GROWTH

5.1. *Damage at* $X_1 \approx h$

Due to the high stresses at $X_1 \approx h$, one of the following can happen: metal cavitation, interface debond and ceramic cleavage. The first two usually do not correspond to the terminal failure of the specimen. Rather, they represent the onset

TABLE 2. *Field quantities pertinent to composite failure: σ_m^* = maximum mean stress in the foil, σ_{22}^* = maximum normal interfacial traction, σ_1^* = maximum principal stress in the elastic substrate, δ_t = crack-tip displacement*

TABLE 2a. $\phi = \pi/6$

$\lvert\mathbf{K}\rvert/(\sigma_0\sqrt{h})$	σ_1^*/σ_0	σ_m^*/σ_0	σ_{22}^*/σ_0	$\delta_t/(\lvert\mathbf{K}\rvert/\sigma_0)^2$
12.30	4.99	3.39	3.57	0.33×10^{-3}
15.06	5.70	3.94	4.11	0.34×10^{-3}
17.30	6.23	4.30	4.44	0.35×10^{-3}
19.68	6.67	4.61	4.77	0.36×10^{-3}

TABLE 2b. $\phi = \pi/4$

$\lvert\mathbf{K}\rvert/(\sigma_0\sqrt{h})$	σ_1^*/σ_0	σ_m^*/σ_0	σ_{22}^*/σ_0	$\delta_t/(\lvert\mathbf{K}\rvert/\sigma_0)^2$
9.01	3.99	2.17	2.28	0.45×10^{-3}
12.05	4.72	2.58	2.68	0.42×10^{-3}
13.63	5.05	2.72	2.81	0.42×10^{-3}
14.58	5.25	2.84	2.91	0.42×10^{-3}

TABLE 2c. $\phi = \pi/3$

$\lvert\mathbf{K}\rvert/(\sigma_0\sqrt{h})$	σ_1^*/σ_0	σ_m^*/σ_0	σ_{22}^*/σ_0	$\delta_t/(\lvert\mathbf{K}\rvert/\sigma_0)^2$
7.38	3.38	1.33	1.40	0.67×10^{-3}
9.10	3.79	1.52	1.57	0.64×10^{-3}
10.44	4.09	1.68	1.71	0.63×10^{-3}
11.67	4.34	1.79	1.83	0.62×10^{-3}

TABLE 2d. $\phi = \pi/2$

$\lvert\mathbf{K}\rvert/(\sigma_0\sqrt{h})$	σ_1^*/σ_0	σ_m^*/σ_0	σ_{22}^*/σ_0	$\delta_t/(\lvert\mathbf{K}\rvert/\sigma_0)^2$
5.74	2.42	0.44	0.31	0.87×10^{-3}
5.96	2.46	0.45	0.31	0.87×10^{-3}
6.21	2.51	0.45	0.32	0.86×10^{-3}
6.37	2.54	0.46	0.32	0.85×10^{-3}

of the progressive damage which leads to the formation of alternate arrays of cavities and intact metal ligaments. The result is a rapidly rising R-curve.

A cavity in an elastic–plastic material grows unstably when the mean stress σ_m reaches a critical value, $C_N\sigma_0$. HUANG *et al.* (1991) carried out a large-deformation analysis of a cavity in an infinite block, which provided the coefficients C_N for a wide

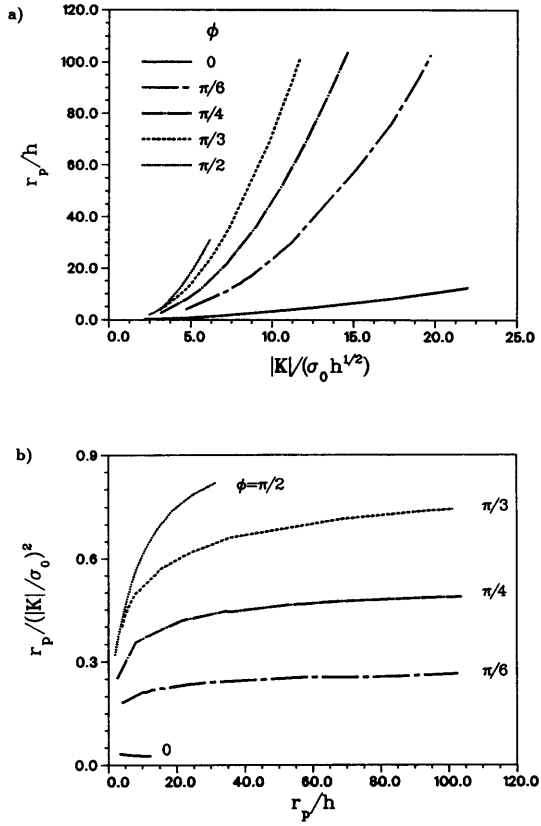

FIG. 10. Mode mixity effect on plastic zone size. (a) Plastic zone size vs remote load. (b) Estimates of $\Lambda(\phi)$ as defined by (15).

range of metals. For example, $C_N = 5.5$ for a metal with properties (2). Substituting $C_N\sigma_0$ for σ^* in (12), we obtain the stress intensity factor required for cavitation

$$\frac{|\mathbf{K}|_c}{\sigma_0\sqrt{h}} = \frac{B_N}{(1/C_N - A_N)}, \tag{17}$$

where A_N and B_N, depending on the loading phase ϕ, are tabulated in Table 1. Since $1/A_N$ is the highest achievable mean stress, the cavitation will not occur if $1/A_N < C_N$. For example, $\sigma_m < 4.5\sigma_0$ when $\phi \geqslant \pi/3$, so that the cavitation will not form at any load level under predominant shear. In other words, $|\mathbf{K}|_c$ increases sharply with the mode mixity (Fig. 12).

Debond occurs when the stress normal to the interface σ_{22} reaches a critical value, $C_A\sigma_0$. Values of C_A in the range 3–10 have been reported for the inclusion–matrix interfaces in steels and Cu–0.6 Pct Cr alloy (ARGON and IM, 1975; CIALONE and ASARO, 1981). The critical $|\mathbf{K}|$ for debond takes the form of (17), with A_N, B_N and C_N replaced by A_A, B_A and C_A, respectively. The loading phase dependent coefficients A_A

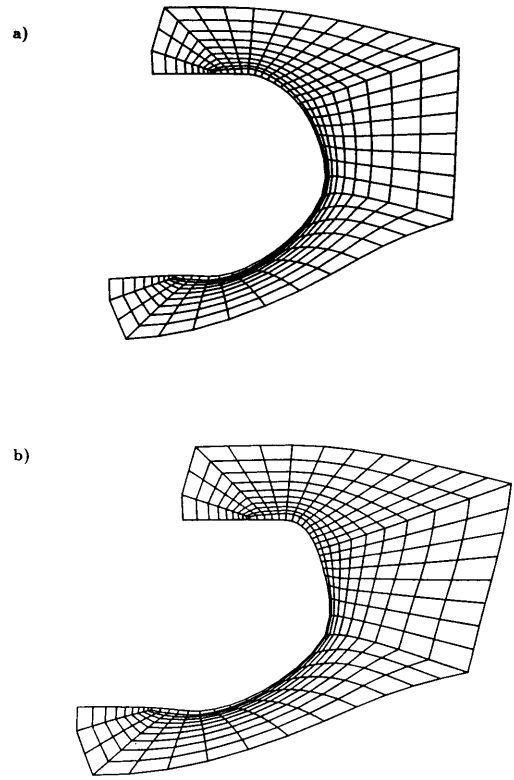

FIG. 11. Deformed crack tips: (a) $\phi = \pi/6$, $\delta_t/b_0 = 2.02$, $|\mathbf{K}|/(\sigma_0\sqrt{h}) = 12.30$; (b) $\phi = \pi/4$, $\delta_t/b_0 = 1.93$, $|\mathbf{K}|/(\sigma_0\sqrt{h}) = 10.59$; (c) $\phi = \pi/3$, $\delta_t/b_0 = 2.12$, $|\mathbf{K}|/(\sigma_0\sqrt{h}) = 9.10$; (d) $\phi = \pi/2$, $\delta_t/b_0 = 1.38$, $|\mathbf{K}|/(\sigma_0\sqrt{h}) = 6.37$.

and B_A are given in Table 1. Figure 13 shows the variation of $|\mathbf{K}|_c$ with ϕ for three values of C_A.

Ceramic fracture occurs when the maximum principal stress in the ceramic, σ^*_1, reaches the critical value $C_C\sigma_0$. The critical $|\mathbf{K}|$ is again given by (17) with the constants appropriate to ceramic fracture. The nominal toughness vs mode mixity is shown in Fig. 14 for several values of ceramic strength C_C.

5.2. *Near-tip crack growth processes*

Upon loading, the blunted crack may grow prior to the cavitation/debond at $X_1 \approx h$. We seek to estimate the load needed for the crack growth. Experimental studies of mixed mode fracture by AOKI *et al.* (1990), TOHGO and ISHII (1990) and COWIE (1989) show that the crack may advance by void nucleation, growth and coalescence in either the blunting or the sharpening region. In the presence of a significant mode I component, the crack advances in the direction of high mean stresses and the fracture surface is covered with the equiaxed dimple pattern. In

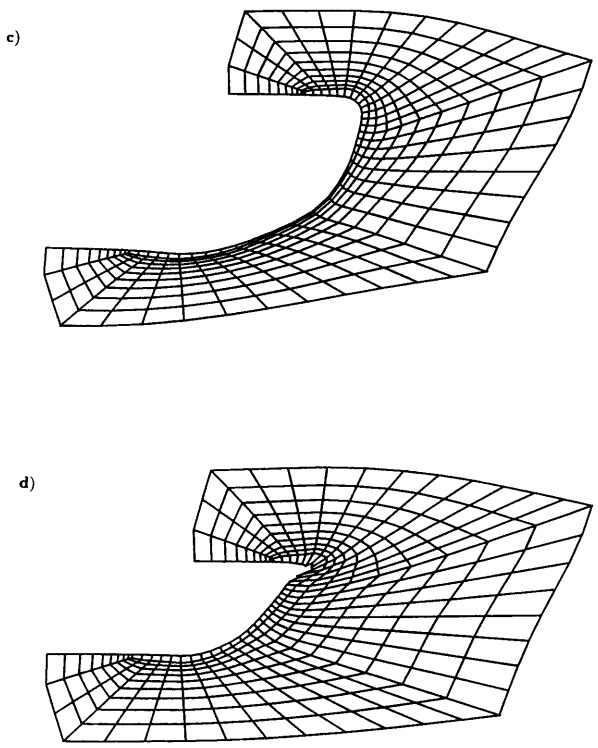

FIG. 11. *Continued.*

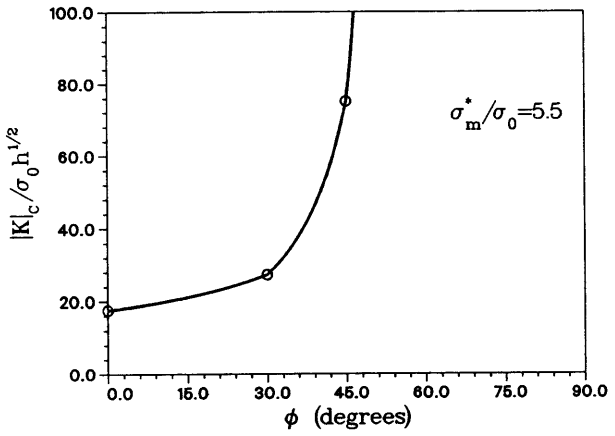

FIG. 12. Variation of nominal fracture toughness with mode mixity if high-triaxiality cavitation is the controlling mechanism.

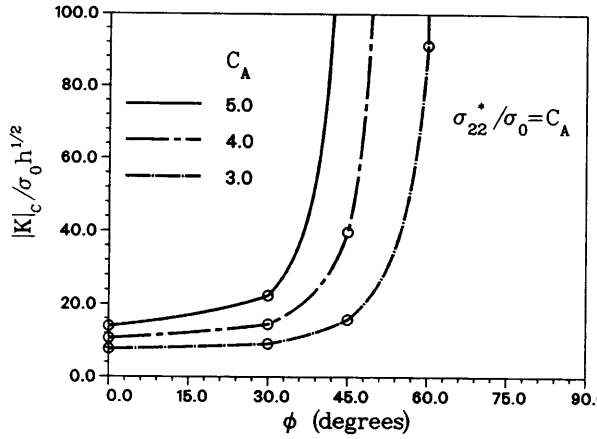

FIG. 13. Variation of nominal fracture toughness with mode mixity of interface debonding is the controlling mechanism. Three values of adhesion strengths are considered.

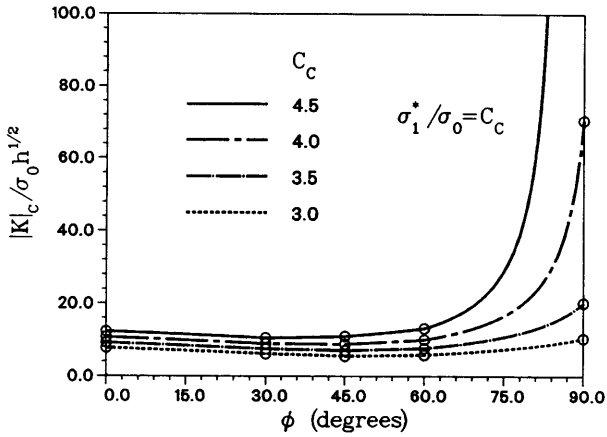

FIG. 14. Variation of nominal fracture toughness with mode mixity if ceramic fracture is the controlling mechanism. Four values of ceramic strengths are considered.

contrast, the crack may advance in the direction of its own plane under predominantly mode II loading. The fracture surface consists of areas of elongated dimples mixed with patches of flat dimple-free surfaces. ARGON *et al.* (1975) have argued that, under mode II dominated deformation, the voids nucleate due to incompatibility effects caused by plastic slip along the crack plane. The low-triaxiality conditions result in the change of void shape rather than volume (FLECK and HUTCHINSON, 1986; FLECK *et al.*, 1989). Consequently, the fracture surface resulting from the coalescence of these voids is relatively smooth, because of the limited void growth and the rubbing between the crack faces. Similar fracture surfaces have also been observed for combined mode I–mode III loading by SCHROTH *et al.* (1987). GIOVANOLA (1988) and

CHO *et al.* (1990) also show that fracture in adiabatic shear bands occurs by a process of void nucleation and coalescence.

MACKENZIE *et al.* (1977) have examined the effect of mean stress on the critical strain to failure. Their experimental data show that the mean stress plays an important role in failure of high-strength steels where voids nucleate soon after first yield and grow with subsequent plastic straining. They observed that the critical strain to failure, $\bar{\varepsilon}_c^p$, shows the same dependence on the mean stress as the rate of void growth (RICE and TRACEY, 1969), i.e. the strain required for failure is increased if the mean stress is decreased. For voids nucleating at large plastic strains, the trend is similar though $\bar{\varepsilon}_c^p$ depends less strongly on the mean stress. The experimental data suggests that the critical strain for fracture should increase as the mode mixity ϕ increases.

Let $\bar{r}(\bar{\varepsilon}^p)$ be the spatial extent of the zone where the equivalent plastic strains are larger than the value $\bar{\varepsilon}^p$. The spatial extent of the zone of large plastic strains is set by δ_t, i.e.

$$\bar{r} = \alpha(\bar{\varepsilon}^p, \phi)\delta_t. \tag{18}$$

Our calculations show that α depends strongly on $\bar{\varepsilon}^p$ but weakly on ϕ. For mode mixities $0 < \phi < \pi/3$ and $\bar{\varepsilon}^p = 0.3$, α ranges between 0.8 and 0.9 when measured in the highly stressed blunting zone. Similarly α varies from 0.4 to 0.5 for $\bar{\varepsilon}^p = 0.6$, and α varies 0.2 to 0.3 for $\bar{\varepsilon}^p = 1.0$. For mode II dominated states, the spatial extent of large strains emanating from the sharpening zone is of interest. Measured in the sharpening zone, $\alpha \approx 2$ for $\bar{\varepsilon}^p = 0.3$ when $\pi/3 < \phi < \pi/2$.

Let X_0 be the mean spacing of second-phase particles. Suppose that the activation of near-tip ductile failure mechanisms requires that $\bar{r}(\bar{\varepsilon}_c^p) = X_0$. Using this in (18) and combining with (16), we get the relation

$$\frac{|\mathbf{K}|_c}{\sigma_0\sqrt{h}} = \sqrt{\frac{E_s/E}{(1-\nu_s^2)\varepsilon_0}}\sqrt{\frac{1}{\alpha(\bar{\varepsilon}_c^p)d}\frac{X_0}{h}}. \tag{19}$$

Our calculations show that the maximum mean stress in the blunting region decreases from $3\sigma_0$ to $1.4\sigma_0$, when the loading changes from mode I to mode II. The mean stress in the sharpening region is even smaller. These results can be used with relation (19) to estimate the dependence of toughness on mode mixity.

As an example, we estimate the ratio $K_C(\phi = \pi/4)/K_{IC}$. Suppose that $\bar{\varepsilon}_c^p$ is 0.3 when $\phi = 0$ and $\bar{\varepsilon}_c^p = 1.0$ when $\phi = \pi/4$. The values of α are 0.81 and 0.27, respectively. From Table 2b and relation (16), $d(\phi = \pi/4) = 0.66$ and $d(\phi = 0) = 0.52$ (VARIAS *et al.*, 1991). Using these values in (19),

$$K_C(\phi = \pi/4)/K_{IC} = \sqrt{0.81 \times 0.52/0.27 \times 0.66} = 1.5.$$

6. CONCLUSIONS

This study provides several results which can be used to assess the competition among the various failure mechanisms. When the foil thickness is sufficiently thin, high-triaxiality cavitation or interface debonding at a distance of several foil thicknesses

ahead of the tip are the mechanisms favored to develop. The critical foil thickness for these mechanisms to develop can be estimated from relations (17) and (19). These relations can guide the choice of foil thickness and other parameters in tailoring the layered system which favors the formation of a large-scale bridging zone and resulting in considerable improvement of the fracture resistance.

Interface tractions and the elevation of the hydrostatic stress are significantly altered by mixed-mode loading. At the same energy release rate, the plastic zone becomes larger as the mode II component increases. Furthermore, the mean stress in the metal layer and the interfacial tractions are greatly reduced. This suggests that the nominal fracture toughness under mixed-mode loading should be larger than that for mode I loading, assuming that failure is controlled by the same mechanism. However, mixed loading has an undesirable consequence—high tensile stresses develop in the ceramic at the interface. Thus ceramic cleavage is increasingly favored as the loading conditions deviate from mode I. The brittle fracture mode can be prevented by making it easier for two other mechanisms to operate: (i) growth of near-tip voids nucleated at second-phase particles and (ii) interface debonding. These two mechanisms can be activated at the desired load levels by controlling the spacing of second-phase particles in the metal, and the spacing of interfacial pores and adhesion strength, respectively. The spacing of interfacial pores can be controlled to a certain degree by processing.

The effect of crack position on fields is discussed in the Appendix. The fields that develop at distances of order h ahead of a crack lying along the lower interface are similar to those for the crack lying in the mid-plane of the foil when $\phi \leqslant 0$ (if the crack lies along the upper interface the similarity is observed for $\phi \geqslant 0$). Thus the relations governing the multi-mechanism competition considered in Section 5 are still applicable.

The fields that prevail at the onset of the damage have been analyzed in this study. As the damage progresses, the stresses redistribute. The formation of multiple debonded zones as the load increases, observed in the experiments of REIMANIS *et al.* (1991), can be studied using a de-adhesion model which takes full account of the stress redistribution following debonding (NEEDLEMAN, 1987; VARIAS *et al.*, 1990). Interfacial pores are also present on the gold–sapphire interfaces of the specimen generated during the bonding process. These are sites of cavity nucleation. A detailed study of the effect of the pores on interfacial failure has been presented by VARIAS (1991).

ACKNOWLEDGEMENT

The authors are grateful to Dr I. E. Reimanis for providing Fig. 1. AGV and CFS are supported by an ONR contract N00014-90-J1380. ZS is supported by an ONR/URI contract N00014-85-K-0883, and by a NSF grant MSS-9011571.

REFERENCES

AOKI, S., KISHIMOTO, K., YOSHIDA, T. and SAKATA, M. 1987 *J. Mech. Phys. Solids* **35,** 431.

AOKI, S., KISHIMOTO, K., YOSHIDA, T., SAKATA, M. and RICHARD, H. A. 1990 *J. Mech. Phys. Solids* **38,** 195.

ARGON, A. S. and IM, J. 1975 *Metall. Trans.* **6A,** 839.
ARGON, A. S., IM, J. and SAFOGLU, R. 1975 *Metall. Trans.* **6A,** 825.
ASHBY, M. F., BLUNT, F. J. and BANNISTER, M. 1989 *Acta metall.* **37,** 1847.
BUDDEN, P. J. 1987 *J. Mech. Phys. Solids* **35,** 457.
BUDDEN, P. J. 1988 *J. Mech. Phys. Solids* **36,** 503.
CHO, K., CHI, Y. C. and DUFFY, J. 1990 *Metall. Trans.* **21A,** 1161.
CIALONE, H. and ASARO, R. J. 1981 *Metall. Trans.* **12A,** 1373.
COWIE, J. G. 1989 U.S. Army Materials Technology Laboratory Report MTL TR 89-20.
FLECK, N. A. and HUTCHINSON, J. W. 1986 *Proc. R. Soc. A* **407,** 435.
FLECK, N. A., HUTCHINSON, J. W. and TVERGAARD, V. 1989 *J. Mech. Phys. Solids* **37,** 515.
GIOVANOLA, H. 1988 *Mech. Mater.* **7,** 73.
HUANG, Y., HUTCHINSON, J. W. and TVERGAARD, V. 1991 *J. Mech. Phys. Solids* **39,** 223.
MACKENZIE, A. C., HANCOCK, J. W. and BROWN, D. K. 1977 *Engng Fracture Mech.* **9,** 167.
MCMEEKING, R. M. 1977 *J. Mech. Phys. Solids* **25,** 357.
NEEDLEMAN, A. 1987 *J. appl. Mech.* **54,** 525.
REIMANIS, I. E., DALGLEISH, B. J. and EVANS, A. G. 1991 *Acta metall.* **39,** 3133.
RICE, J. R. 1968 *J. appl. Mech.* **35,** 379.
RICE, J. R. and JOHNSON, M. A. 1970 In *Inelastic Behavior of Solids* (edited by M. F. KANNINEN, W. F. ADLER, A. R. ROSENFIELD and R. I. JAFFEE), p. 641. McGraw-Hill, New York.
RICE, J. R. and TRACEY, D. M. 1969 *J. Mech. Phys. Solids* **17,** 201.
SCHROTH, J. G., HIRTH, J. P., HOAGLAND, R. G. and ROSENFIELD, A. R. 1987 *Metall. Trans.* **18A,** 1061.
SHIH, C. F. 1974 *Fracture Analysis*, ASTM STP 560, p. 187.
SHIH, C. F. 1981 *J. Mech. Phys. Solids* **29,** 305.
SUO, Z., BAO, G. and FAN, B. 1992 *J. Mech. Phys. Solids* **40,** 1.
TOHGO, K. and ISHII, H. 1990 *Proceedings of* 1990 *KSME/JSME Conference on Fracture and Strength*, Seoul.
VARIAS, A. G. 1991 Ph.D. thesis, Brown University.
VARIAS, A. G., O'DOWD, N. P., ASARO, R. J. and SHIH, C. F. 1990 *Mater. Sci. Engng* **A126,** 65.
VARIAS, A. G., SUO, Z. and SHIH, C. F. 1991 *J. Mech. Phys. Solids* **39,** 963.

APPENDIX

DEVELOPMENT OF HIGH STRESSES AHEAD OF AN INTERFACE CRACK

The effect of the crack position on the fields in the foil and its vicinity is discussed in this Appendix. The crack lies along the lower interface. The origin of the coordinate system is

positioned at the crack tip and the X_1-direction is parallel to the interfaces. The formulation of the boundary value problem is similar to that described in Section 2. Tractions consistent with mixed-mode elastic crack-tip field of a homogeneous material under plane strain conditions are applied at large distances compared to the layer thickness h. The cases examined are $\phi = -\pi/4$, 0 and $\pi/4$. The material properties are given by the values in (2).

Figure A1(a) shows contours of the effective plastic strain for $|\mathbf{K}|/(\sigma_0\sqrt{h}) = 14.58$ and $\phi = -\pi/4$. The magnitude of the applied load is identical to that applied to the centerline crack problem in Fig. 5, but the phase angle is of opposite sign. Consequently it is appropriate to compare the deformation patterns above the interface crack in Fig. A1(a) with the deformation patterns below the crack-line in Fig. 5(a). Indeed the similarity of the strain distributions in these regions is striking. Note that the plastic deformation in the X_2-direction are constrained in like manner in both cases. Figure A1(b) shows the distribution of the mean stress. High stresses develop along the upper interface at a distance h ahead of the crack tip. These levels are similar to those along the lower interface at the same distance ahead of the centerline crack [see Fig. 5(b)]. The distribution of the normal interfacial traction along the upper interface shown in Fig. A1(b) ($X_2 = h$) is also quite similar to that at the lower interface ($X_2 = -h/2$) of the centerline crack. The maximum tensile stress in the ceramic bonded to the upper interface ($X_2 = h$) is about 10% lower than that for the centerline crack.

The fields for the interface crack for $\phi = 0$ have also been examined. The distribution of the fields is very much like that for the mode I centerline crack which is discussed in VARIAS *et al.* (1991). The interested reader is referred to that article for details.

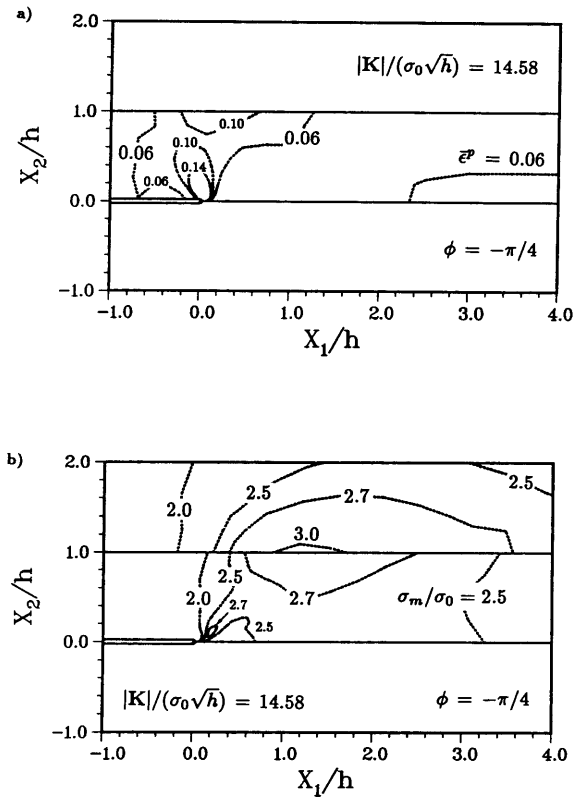

FIG. A1. Contours of: (a) effective plastic strain, and (b) stress triaxiality. $\phi = -\pi/4$, $|\mathbf{K}|/(\sigma_0\sqrt{h}) = 14.58$. Interface crack.

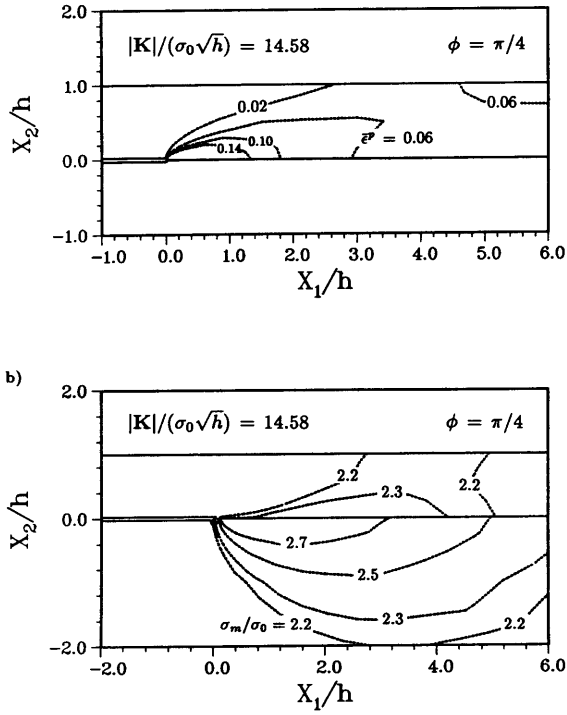

FIG. A2. Contours of: (a) effective plastic strain, and (b) stress triaxiality. $\phi = \pi/4$, $|\mathbf{K}|/(\sigma_0\sqrt{h}) = 14.58$. Interface crack.

Figure A2 shows the contours of the effective plastic strain and the mean stress for $|\mathbf{K}|/(\sigma_0\sqrt{h}) = 14.58$ and $\phi = \pi/4$. The strain contours in Fig. A2(a) bear some resemblance to the patterns above the centerline crack in Fig. 5(b). The maximum mean stress in the foil in Fig. A2(b) is about 20% lower than that for the centerline crack [see Fig. 5(a)] or that for the interface crack for $\phi = -\pi/4$ [see Fig. A1(b)]. The maximum normal interfacial traction is also smaller by the same amount. In contrast the maximum principal stress in the ceramic is about 10% larger than that for the centerline crack; this maximum develops very close to the tip of the interface crack.